CrossMark

Analysis of the Corrosion Behavior of an A-TIG Welded SS 409 Weld Fusion Zone

R.S. Vidyarthy and D.K. Dwivedi

AISI 409 (SS 409) ferritic stainless steel is generally used as the thick gauge section in freight train wagons, in ocean containers, and in sugar refinery equipment. Activating the flux tungsten inert gas (A-TIG) welding process can reduce the welding cost during fabrication of thick sections. However, corrosion behavior of the A-TIG weld fusion zone is a prime concern for this type of steel. In the present work, the effect of the A-TIG welding process parameters on the corrosion behavior of a weld fusion zone made of 8-mm-thick AISI 409 ferritic stainless-steel plate has been analyzed. Potentiodynamic polarization tests were performed to evaluate the corrosion behavior. The maximum corrosion potential (E_{corr}) was shown by the weld made using a welding current of 215 A, a welding speed of 95 mm/min, and a flux coating density of 0.81 mg/cm^2. The minimum E_{corr} was observed in the weld made using a welding current of 190 A, a welding speed of 120 mm/min, and a flux coating density of 1.40 mg/cm^2. The current study also presents the inclusive microstructure–corrosion property relationships using the collective techniques of scanning electron microscopy, energy-dispersive x-ray spectroscopy, and x-ray diffraction.

1. Introduction

AISI 409 (SS 409) is a titanium stabilized ferritic stainless steel (FSS) with 10% Cr-12% Cr, and it is generally used in chemical and industrial plants due to the material's good corrosion resistance (Ref 1-4). SS 409 was initially developed for material handling equipment used in corrosive environments, such as in the wagons of a freight train and in automotive exhaust mufflers. Moreover, there are various potential applications for the low-cost corrosion resistance of SS 409 stainless steel, such as in ocean containers and in sugar refinery equipment (Ref 5, 6). Many of these applications involve the fabrication of steel with thick gauge sections (> 3 mm).

Gas tungsten arc welding (GTAW) is widely used for welding SS 409 using austenitic filler wire (Ref 7). Previously reported works suggest that the heat-affected zone (HAZ) of the SS 409 shows susceptibility to intergranular corrosion (IGC) attack (Ref 5, 8-10). It was also reported that intersecting isotherms, obtained during multi-pass welding, could promote HAZ sensitization to IGC (Ref 11). Thick gauge sections that require multiple passes to form the conventional GTAW joint will naturally have overlapping weld beads with an intersecting isotherm, which could be more susceptible to IGC. Anttila et al. (Ref 7) reported that the compositional difference due to the filler between the base metal and the weld bead may lead to the premature failure of the component in a sulfuric environment.

The A-TIG welding process can easily weld thick sections up to 12 mm in a single pass without any filler wire (Ref 12). Arc constriction (Fig. 1a) and reversal in Marangoni convection (Fig. 1b) are the most accepted mechanisms for deep and narrow weld penetration in A-TIG welding compared to conventional GTAW (Ref 12-14). It is expected that a single-pass A-TIG welding process could suppress the problems of intersecting isotherms and chemical inhomogeneity. Additionally, the performance of A-TIG weld joints was reported to be more attractive compared to multi-pass GTAW weldments in many applications (Ref 15). However, Kapilashrami et al. (Ref 16) doubted that the A-TIG weld fusion zone could have inferior corrosion properties due to the use of flux during A-TIG welding.

After an exhaustive study of the available literature on A-TIG welding, it was observed that the response of the A-TIG weld fusion zone to corrosion has not yet been explored. Therefore, attempts were made to study the corrosion behavior of A-TIG weld fusion zones that were made with varying process parameters such as the welding current, the welding speed, and the flux coating density.

2. Material and Experimental Procedure

SS 409 plates used in the present work were supplied by the Indian railway. The chemical composition and mechanical properties of the as-received base metal are presented in Tables 1 and 2, respectively. The base metal plates were machined to prepare specimens of size $150 \times 40 \times 8$ mm^3. SiO_2 was used as an activating flux. The flux was mixed with acetone and then coated over the plate surface using an electric spray gun. Flux quantity coated per unit surface area of the plate has been referred as flux coating density in the current work. Each specimen was duplicated and weighed to ensure consistency of the flux coating density. For A-TIG welding, a direct current electrode negative (DCEN) power source was

R.S. Vidyarthy and **D.K. Dwivedi**, Department of Mechanical and Industrial Engineering, Indian Institute of Technology Roorkee, Roorkee, Uttrakhand 247667, India. Contact e-mail: vidyashanker01@gmail.com.

attached with the water-cooled torch having 2% thoriated tungsten electrode of 2.9 mm diameter. Copper backing and side support were used to protect the plate from any kind of overheating Fig. 2(a).

Central composite design (CCD) was used to prepare the design matrix. Three factors, namely welding current, welding speed, and flux coating density with five levels, were considered as the input variables (Table 3). On the basis of design matrix, 'bead-on-plate' welds were made along the centerline of the plate (Fig. 2b). Samples for metallographic examination were prepared using standard metallographic procedures including mounting, grinding, and polishing. The polished specimens were etched using Vilella's reagent (1 g picric acid + 5 mL hydrochloric acid + 100 mL ethanol). The base metal grain size was measured with the help of line intersection method as per 'ASTM E112-12' standard using FESEM images. The welded samples before and after corrosion test were characterized using stereomicroscope (Nikon SMZ 745T), energy-dispersive x-ray spectroscopy (EDS)-assisted field emission secondary electron microscope (FESEM), and x-ray diffraction (XRD).

Samples after macroscopic and microscopic analysis were again cloth-polished to remove the etching effect from the surface before the corrosion test. Potentiodynamic polarization test was performed in 3.5% NaCl solution for analyzing the corrosion behavior of the A-TIG weld fusion zone. Potentiodynamic polarization tests were performed at room temperature. Gamry potentiostat (interface 1000) of three electrodes system consisting of a reference electrode (saturated calomel electrode: SCE), a working electrode (WE), and one graphite counter electrode (CE) was used. The potentiodynamic polarization test was conducted at a scan rate of 1 mV/s within the voltage range of ± 1.5 V. The exposed surface area was kept 0.15 cm^2 in all cases. A solution of nitrocellulose and ethyl acetate was used to shield the rest of the part of the weld fusion zone to avoid any kind of electrochemical reaction.

3. Results

3.1 Potentiodynamic Polarization Test

During the corrosion test of the weld fusion zone in a 3.5% NaCl solution, anodic (Fe → Fe^{2+} + 2e$^-$) and cathodic
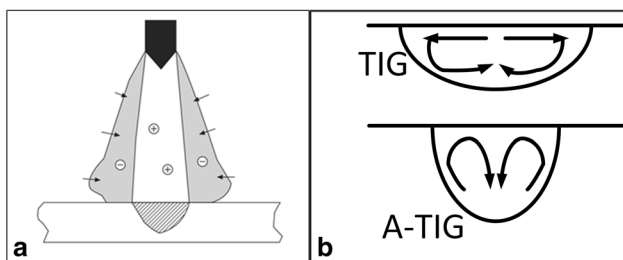
Fig. 2 (a) A-TIG welding setup and (b) bead-on-plate welds

Fig. 1 Schematics of (a) the arc constriction and (b) weld pool flow direction during GTAW and A-TIG welding process

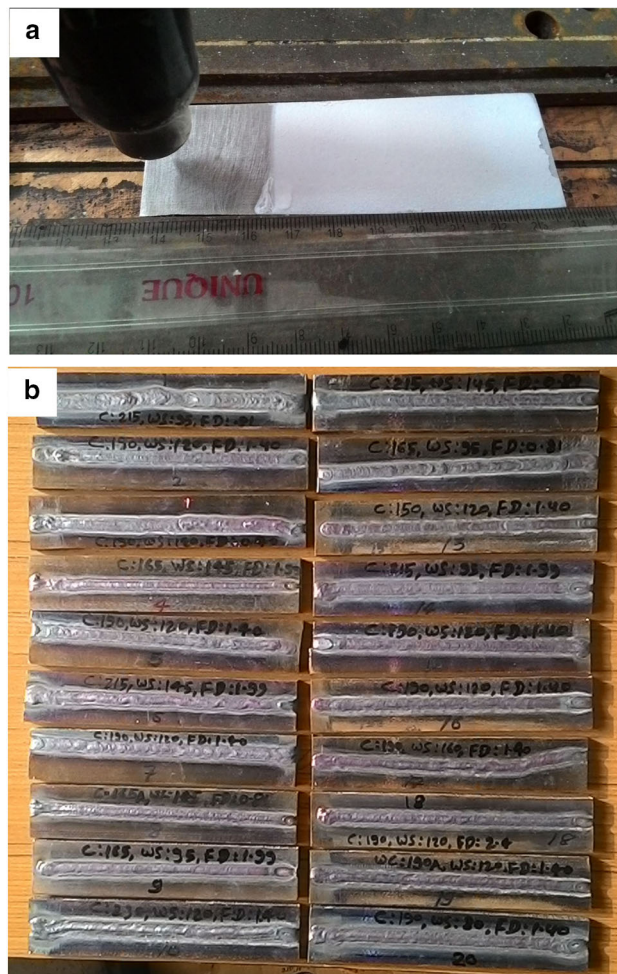**Table 1 Chemical composition of the base material and the A-TIG weld fusion zone**

Elements, wt.%	C	Si	Mn	P	S	Cr	Ni	Mo	Ti	Fe
Base	0.009	0.51	0.82	< 0.005	0.018	10.4	0.33	0.023	< 0.002	Balanced
Weld metal	0.074	0.57	0.813	< 0.005	0.015	10.6	0.248	0.015	< 0.002	Balanced

Table 2 Mechanical properties of the base material

UTS	Yield stress (offset 0.2%)	Tensile strain, %		Microhardness, VHN	Impact energy, J
		At maximum load	At break		
443.56 ± 12, MPa	240 ± 8, MPa	19.32 ± 2	32.59 ± 1.5	165 ± 11	75 ± 5

Table 3   Welding process parameters and their levels

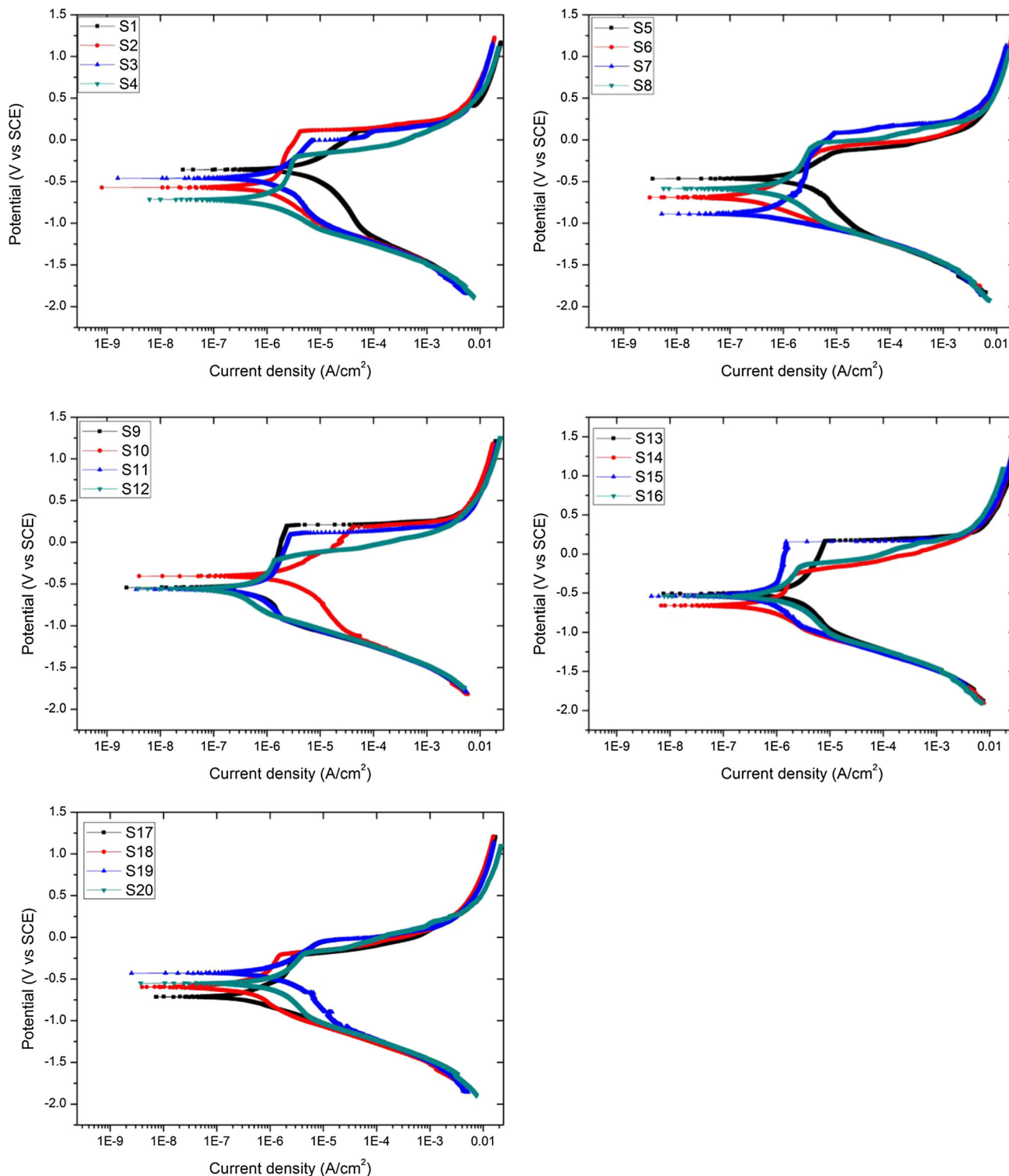| Welding process parameters	Unit	Levels				
		− 2	− 1	0	1	2
Welding current, I	Amps	150	165	190	215	230
Welding speed, S	mm/min	80	95	120	145	160
Flux coating density, F	mg/cm^2	0.40	0.81	1.40	2.0	2.40

Fig. 3   Tafel fitting curves of the different sample obtained from potentiodynamic polarization test

Table 4 Developed design matrix with the respective responses

| Run no. | Sample identification | Process parameters | | | Heat input, J/mm | Responses | |
		I, Amp	S, mm/min	F, mg/cm²		Corrosion rate, mpy	E_{corr}, mV
1	S1	215	95	0.81	1642.51	1.198	− 358
2	S2	190	120	1.40	1097.04	3.815	− 572
3	S3	190	120	0.40	1097.04	2.547	− 461
4	S4	165	145	1.99	742.91	5.59	− 713
5	S5	190	120	1.40	1097.04	4.991	− 466
6	S6	215	145	1.99	1076.13	3.7738	− 689
7	S7	190	120	1.40	1097.04	4.435	− 890
8	S8	165	145	0.81	742.91	4.7477	− 581
9	S9	165	95	1.99	1133.91	2.6765	− 544
10	S10	230	120	1.40	1421.83	1.063	− 406
11	S11	215	145	0.81	1076.13	2.1856	− 566
12	S12	165	95	0.81	1133.91	2.4181	− 557
13	S13	150	120	1.40	788.68	4.085	− 508
14	S14	215	95	1.99	1642.51	1.368	− 661
15	S15	190	120	1.40	1097.04	4.35	− 541
16	S16	190	120	1.40	1097.04	4.7435	− 542
17	S17	190	160	1.40	822.78	4.9132	− 715
18	S18	190	120	2.40	1097.04	4.871	− 596
19	S19	190	120	1.40	1097.04	4.61	− 431
20	S20	190	80	1.40	1645.55	1.537	− 550
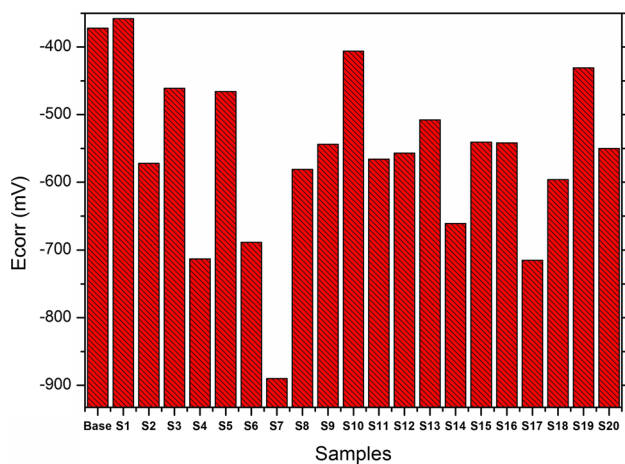
Fig. 4 E_{corr} values of the as-received base metal and A-TIG weld samples
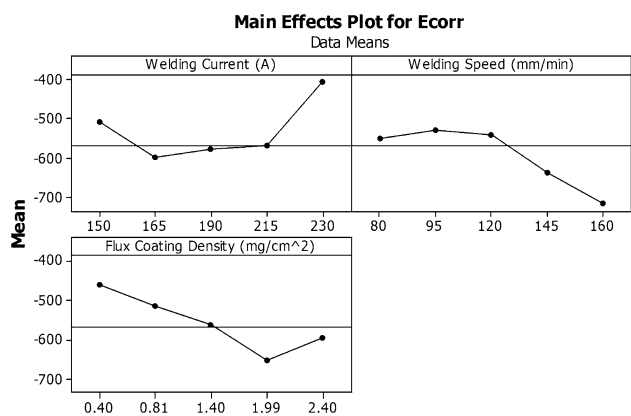

Fig. 5 Effect of welding process parameters on E_{corr}: (a) welding current, (b) welding speed, and (c) Flux density
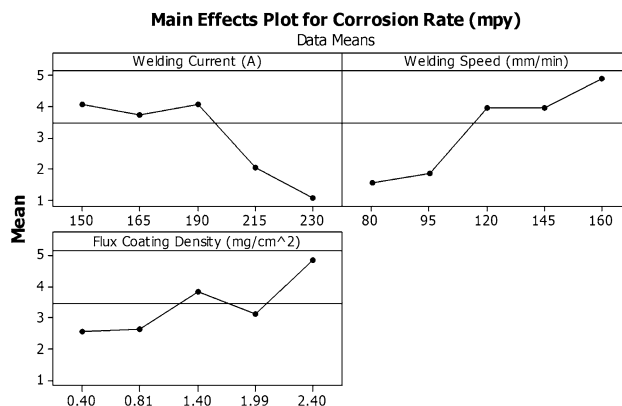

Fig. 6 Effect of welding process parameters on corrosion rate (mpy): (a) welding current, (b) welding speed, and (c) Flux density

$(O_2 + 2H_2O + 4e^- \rightarrow 4OH^-)$ corrosion reactions occurred at the surface exposed to the electrolyte solution (Ref 17). The anodic and cathodic polarization behavior of the welds was obtained using potentiodynamic polarization studies. The corrosion rate was calculated using Eq 1, which assumes that i_{corr} is distributed over the entire wetted area (Ref 18).

$$CR = \frac{0.1288 \times 10^{-3} \times i_{corr} \times EW}{D} \quad \text{(Eq 1)}$$

where CR, EW, and D represent the corrosion rate, the equivalent weight, and the density of the material, respectively.

Tafel curves generated during the potentiodynamic polarization tests are shown in Fig. 3. The corrosion potential (E_{corr}) and the corrosion rate were measured from the Tafel curve fitting (Table 4). For the ease of discussion, identification names were given to the test samples based on the run number. The minimum E_{corr} value of − 890 mV and the maximum E_{corr} value of − 358 mV were observed in samples S7 and S1, respectively. The minimum corrosion rate of 1.068 mpy and the maximum corrosion rate of 5.59 mpy were obtained in samples
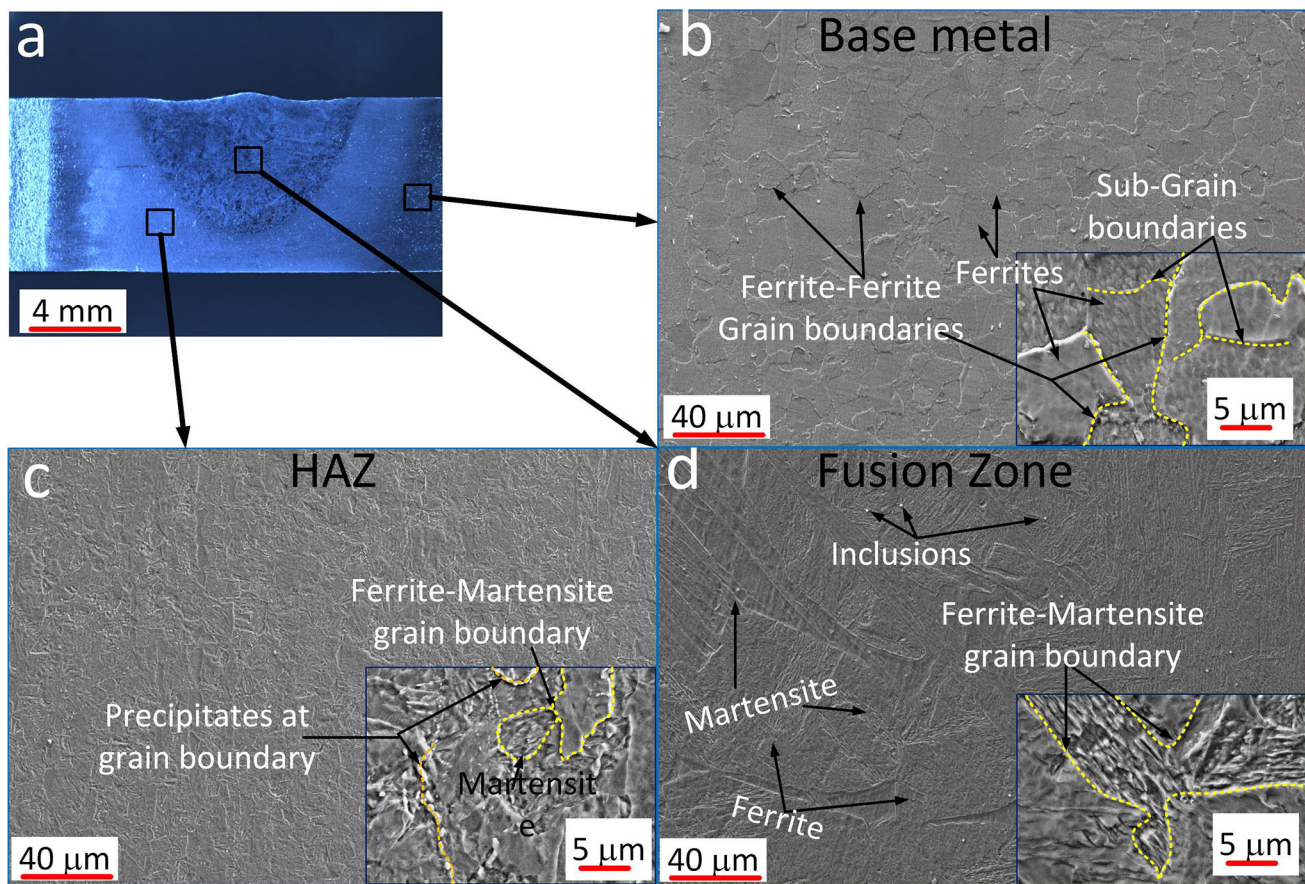
Fig. 7 (a) Schematic of A-TIG weld cross section, (b) microstructure of the as-received base metal, (c) A-TIG HAZ, and (d) A-TIG weld fusion zone

S7 and S1, respectively. The corrosion rate was in good agreement with the E_{corr} values. It was also observed that all the A-TIG weld fusion zone samples, except S1, had a lower E_{corr} value than the corresponding value for the base metal (Fig. 4), which indicates that the corrosion resistance of the material was degraded after the welding process. Niekerk et al. (Ref 2) also reported the degradation in corrosion resistance due to welding.

The main effects plot for the E_{corr} and the corrosion rate with the welding current, the welding speed, and the flux coating density is shown in Fig. 5 and 6, respectively. The input process parameters are depicted along the X-axis, and the desired responses are on the Y-axis. The E_{corr} values were found to decreased initially with an increase in the welding current from 150 to 165 A, and afterward, it increased with an increase in welding current (Fig. 5a). The increase in the welding speed (Fig. 5b) and the flux coating density (Fig. 5c) resulted in a decreased E_{corr} value. Main effects plot for corrosion rate (Fig. 6a) suggests that an increase in the welding current results in a decreased corrosion rate. However, the corrosion rate was found to increase with the welding speed and the flux coating density (Fig. 6b and c). The effect of heat input on the corrosion rate was also investigated and is presented in Fig. 6. The heat input was calculated using $H = \frac{I \times V}{S} \times \eta$ where H = heat input per unit weld length (J/mm), I = welding current (A), V = welding voltage (V), S = welding speed (mm/s), and η = arc efficiency. The arc efficiency for all the welding was assumed 75%. The welding voltage was considered the same for the varying flux coating densities. A marginal increase

in the corrosion rate was observed initially with an increase in heat input. Afterward, however, a significant decrease in the corrosion rate was noticed.

3.2 Microstructure

3.2.1 As Welded Condition. The cross section of an A-TIG weld is comprised of unaffected base metal, the heat-affected zone (HAZ), and the weld fusion zone (Fig. 7a). A fully ferritic grain distribution was observed in the unaffected base metal (Fig. 7b). Ferrite–ferrite primary and subgrain boundaries were observed in the base metal. An average grain size of 25 ± 5 μm was measured in the base metal. Ferritic grains with martensitic transformations were observed at the grain boundary in the HAZ (Fig. 7c). Intermetallic precipitates were also detected on the grain boundaries (Fig. 7c inset). Delta ferrite with acicular martensite was observed in the A-TIG weld fusion zone (Fig. 7d). Inclusions in the grain matrix were also observed. Optical emission spectroscopy was performed to analyze the chemical composition of the weld fusion zone (Table 1). It was observed that the chemical composition of the weld metal was not significantly affected by the flux. Minor variation in the chemical composition could be attributed to the precipitation of intermetallic phases and slag formation during welding (Ref 15).

3.2.2 After Corrosion Test. Large numbers of wide and shallow pits were observed at the corroded surface of the as-received base metal (Fig. 8a). Most of them were linked
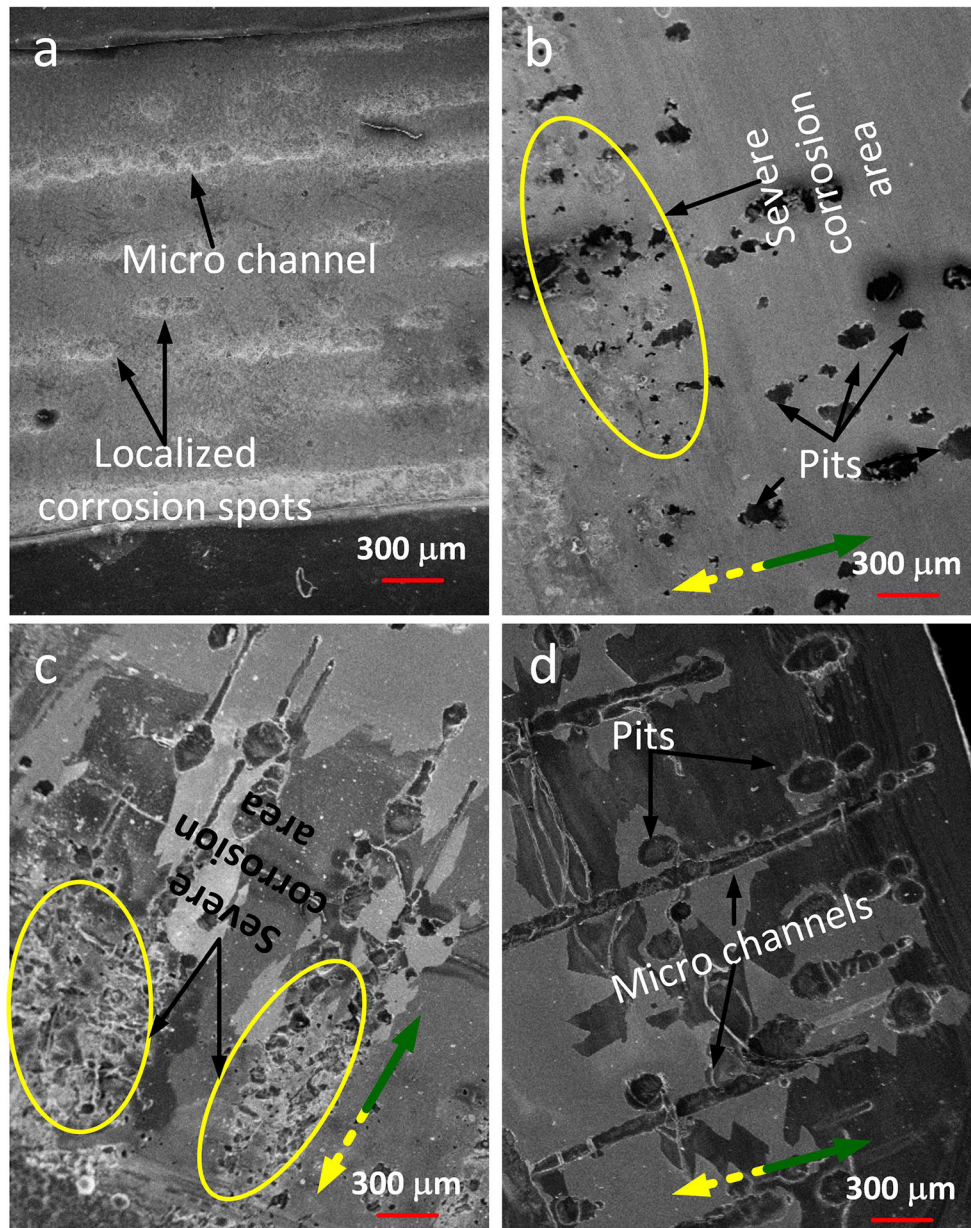
Fig. 8 Macro of the corroded surface of (a) base metal, (b) S4, (c) S7, and (d) S10; arrows direction of the doted yellow and green lines indicating toward and away from the weld fusion boundary, respectively (Color figure online)

together and formed unidirectional microchannels. Micrographs of the corroded surfaces of the weld fusion zone were collected at low magnification and are shown in Fig. 8(b), (c), and (d). The yellow and green arrows indicate the area that approaches the weld fusion line and the weld-top surface, respectively. Severe corrosion was observed near the shielded area in the side of the weld fusion boundary (Fig. 8b and d). An extremely localized and an intense attack produced pits in the weld fusion zone (Fig. 8b, c, and d). Deep and narrow pits were observed in the sample S4, while wide and shallow pits were observed in samples S7 and S10. Taillike microchannels were observed on the corroded surface of sample S7, while continuous, narrow, and long microchannels were observed on sample S10.

Severely corroded zones and pits were further analyzed with the help of an EDS-assisted electron microscope (Fig. 9 and 10). Deep and dark cavities were observed between the grain

matrices in the severely corroded zone (Fig. 9b). The presence of deep and dark cavities between the grain matrices could be attributed to the dissolution of the grain boundary. Pits were also seen in the ferrite matrix near the ditched grain boundaries. EDS maps of the selected areas of the corroded surfaces indicated the absence of chromium in the cavity (Fig. 9c, e, and f). Niekerk et al. (Ref 2, 18, 19) depicted this kind of grain separation, in the form of a continuous cavity along the grain boundary, as grain boundary ditching. A complete grain ditching suggests the possibility of (Fig. 9b). IGC is a selective attack that occurs near the grain boundaries of the ferrous or nonferrous materials. In ferritic stainless steel, chromium-rich carbides, such as $Cr_{23}C_6$ and Cr_7C_3, form on the grain boundaries due to supersaturation in the carbon (Ref 20–22). The formation of precipitates was confirmed through XRD analysis (Fig. 11). Consequently, this resulted in the chromium-
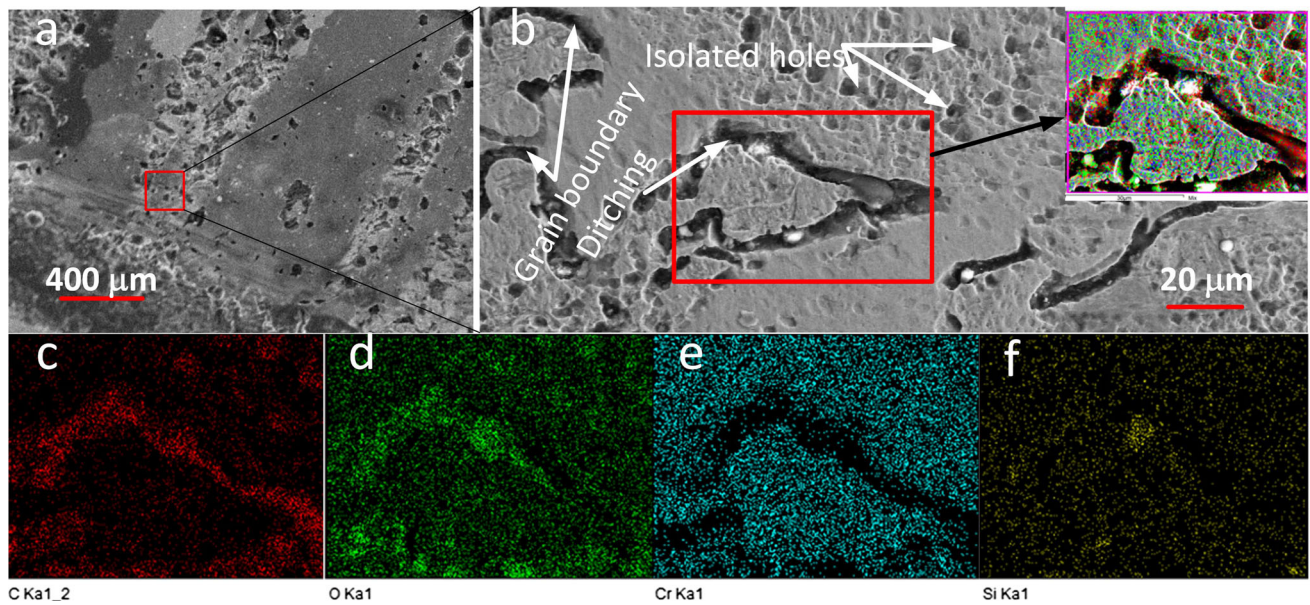
Fig. 9 Micrographs of (a) the severely corroded zone, (b) grains structure, and (c-f) EDS elemental maps of the selected area in (b)
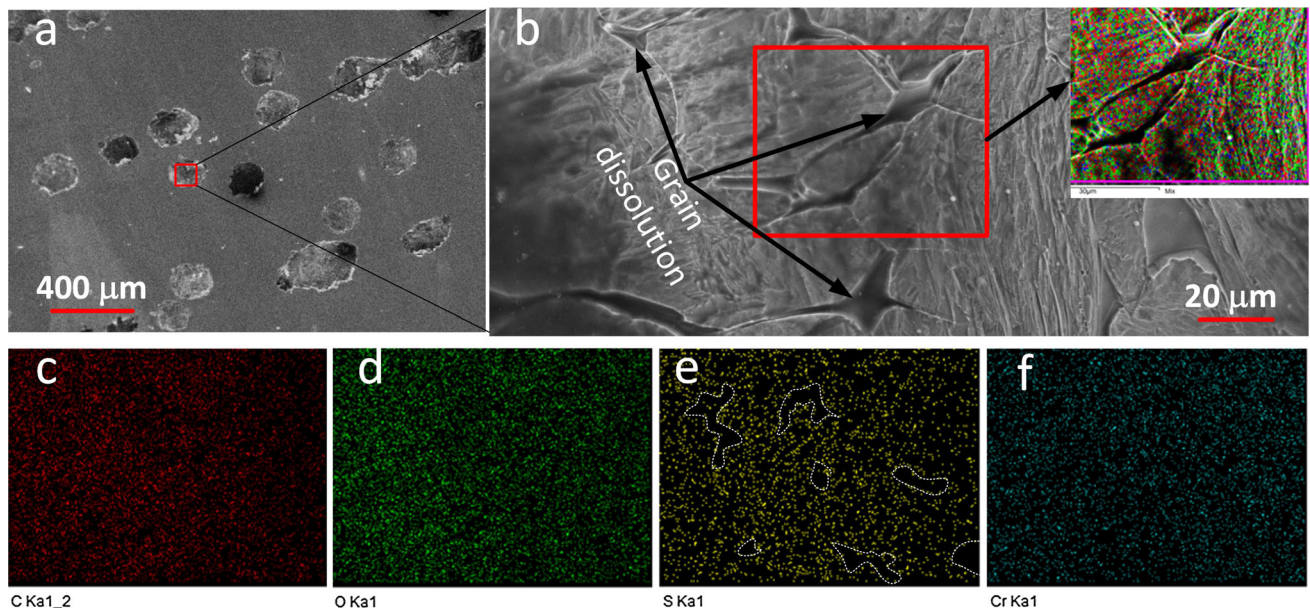

Fig. 10 Micrographs of (a) the pits on the surface, (b) grains structure within the pit, and (c-f) EDS elemental maps of the selected area in (b)

depleted zone that is adjacent to the chromium-rich carbide layers. The chromium-depleted zone in ferritic stainless steel was highly susceptible to the corrosion attack. During the potentiodynamic polarization tests, the sensitized grain boundary acted as an anode compared to the rest of the surface (Ref 23). This resulted in the formation of ditches between the grain matrices (Fig. 9b). Elemental distribution analysis of the corroded surface near the fusion line also suggests the presence of IGC (Fig. 9c, e, and f).

Complete grain boundary separation was not observed in the pit (Fig. 10b). However, some craterlike structures were detected. This type of crater could be attributed to the complete dissolution of the small grain matrix during corrosion. EDS maps indicate a uniform distribution of all the elements (Fig. 10c, e, and f). A minor discontinuity was observed in

the sulfur matrix (Fig. 10d). This may be attributed to the presence of oxide/sulfide inclusions in the A-TIG weld fusion zone. Sulfide inclusions in the ferrite matrix helped to form the galvanic couple. In the presence of salted water, the sulfur-rich matrix acted as an anode, while the matrix without sulfur acted as a cathode (Ref 24). The oxide and sulfide inclusions in the A-TIG weld fusion zone were confirmed through XRD analysis (Fig. 11).

4. Discussion

The severe corrosion attack was observed near the fusion line, whereas comparably reduced corrosion with pitting
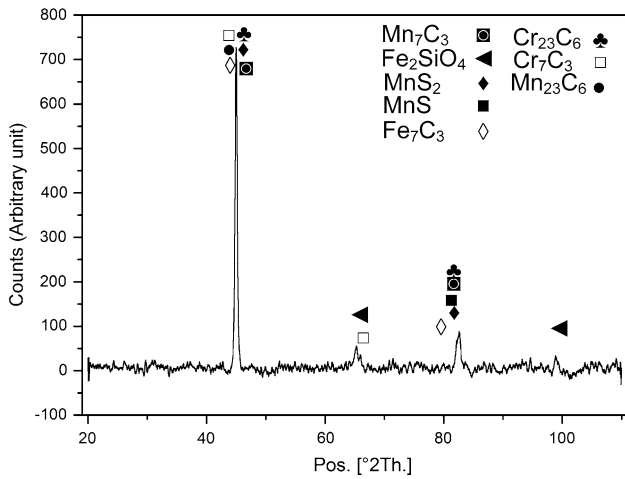
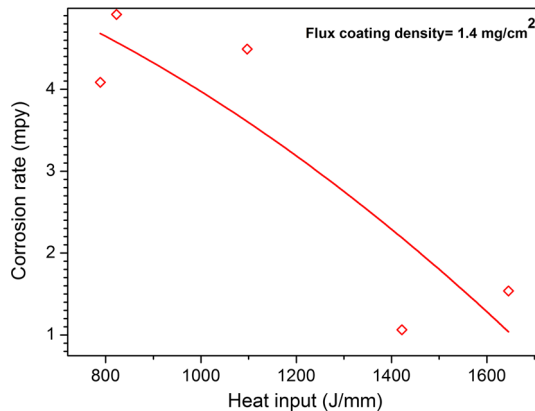**Fig. 11** XRD spectrum of the A-TIG weld fusion zone

Fig. 12 Effect of heat input on the corrosion rate

dominated the weld center. Chromium-depleted regions adjacent to the Cr-rich carbides, such as $Cr_{23}C_6$ and Cr_7C_3, were the primary locations for the corrosion attack. The presence of $Cr_{23}C_6$- and Cr_7C_3-based carbide precipitates in the A-TIG weld fusion zone was confirmed by XRD analysis (Fig. 11). Cr-rich carbides primarily precipitated on the grain boundaries because of the lower energy required for precipitation and nucleation at the grain boundaries. The chromium-rich phase, Cr_2N, could affect the corrosion behavior, but Cr_2N was not detected in the A-TIG weld fusion zone during the XRD (Fig. 11) and EDS (Fig. 13) analyses. A negligible amount of nitrogen in the as-received base metal might be the reason for the absence of Cr_2N. Vitek et al. (Ref 25) also reported that Cr_2N precipitates were not observed in the 12Cr-1Mo-V-W steel that possessed a nitrogen concentration below 0.05%.

Sensitization due to chromium depletion occurs by holding or cooling the weld to a temperature range between 425 °C and 700 °C (Ref 26). Carbide precipitation in FSS is thought difficult to avoid due to the low-carbon solubility and the rapid chromium diffusion rate. However, it could be desensitized if chromium diffuses back to the depleted grain boundary areas (Ref 10, 11). Near the fusion line, the cooling rate in the desensitization temperature range (from 900 to 700 °C) was supposed to high enough. So, the diffusion of the chromium back into the matrix was reduced. But near the weld center, sufficient time was available for the diffusion of chromium

back into the ferrite matrix. Diffusion of chromium back into the matrix healed the fusion zone and resulted in a relatively desensitized structure.

Heat input also affects the sensitivity of the weld fusion zone through the cooling rate during welding. A relation between the corrosion rate and the heat input with a constant flux coating density suggested that the corrosion rate decreased as the heat input was increased (Fig. 12). According to Rosenthal's heat flow equation, the greater the heat input, the lower the cooling rate should be as indicated in Eq 2 (Ref 25). So, the time for chromium back diffusion in ferrite would be greater; hence, the corrosion attack should be suppressed. Kim et al. (Ref 26) and Greeff (Ref 27) also proposed that increases in the heat input during single-pass welding reduce the material's sensitivity to corrosion attacks.

$$\text{Cooling Rate} \propto \frac{1}{(q/v)^2} \qquad \text{(Eq 2)}$$

where q is heat input and v is welding speed.

The pitting mechanism was almost same as for crevice corrosion but in a more localized way. EDS analysis of the inclusions present in the A-TIG weld fusion zone is shown in Fig. 13. Spectrum 1 and spectrum 2 show the presence of sulfide and oxide inclusions, while spectrum 3 shows an oxide inclusion. A fraction of the flux (SiO_2) used was mixed in the weld pool to produce active oxygen [O] during the A-TIG welding process, which formed metallic or non-metallic oxides (Ref 29). Non-metallic inclusions, like sulfides and complex sulfide-oxide inclusions, and second phase precipitates created inhomogeneity in the weld fusion zone. These yielded weaker spots in the passive film, and hence, they decreased the corrosion resistance. The flux coating density may be directly responsible for the oxide inclusion content in the weld fusion zone, which leads to a lower corrosion resistance. The nature of the inclusions was also confirmed through XRD analysis (Fig. 11). Differences in the thermal expansion coefficients and the chemical reactivity between the inclusions and the metal matrix inclusions also affected the corrosion behavior of the weld fusion zone (Ref 28-30).

A non-metallic inclusion, like manganese sulfide (MnS), has a higher coefficient of thermal expansion than the metal matrix, which may lead to the formation of a crevice after cooling. Inclusions like SiO_2 have a lower coefficient of thermal expansion compared to the metal matrix, which could lead to the development of textural stresses around the inclusion. Inclusions having a greater potential difference than the metal matrix provides an environment for that is ideal for galvanic coupling. During the corrosion process, the sulfur-infected matrix close to the sulfide inclusion acts as an anode, while the matrix without sulfur acts as a cathode. The active sulfides also act as cathodic sites during galvanic coupling. The various types of inclusions and heterogeneities that are generally reported for steel weld fusion zone surfaces can be organized in increasing order of their pitting susceptibilities as follows (Ref 31).

$$\text{Oxides} <\,<\,< \text{ Grain boundaries} < (Mn, Cu)S <$$
$$(Mn, Fe)S < MnS + Al_2O_3 < MnS(Mn, Cr)S$$
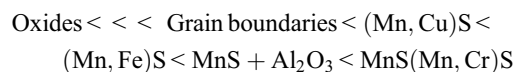
The above sequence for pitting susceptibilities indicates that corrosion behavior in the A-TIG weld fusion zone was affected more by the sulfide inclusions than the oxide inclusions. Hence, it could be concluded that the presence of oxide inclusions,
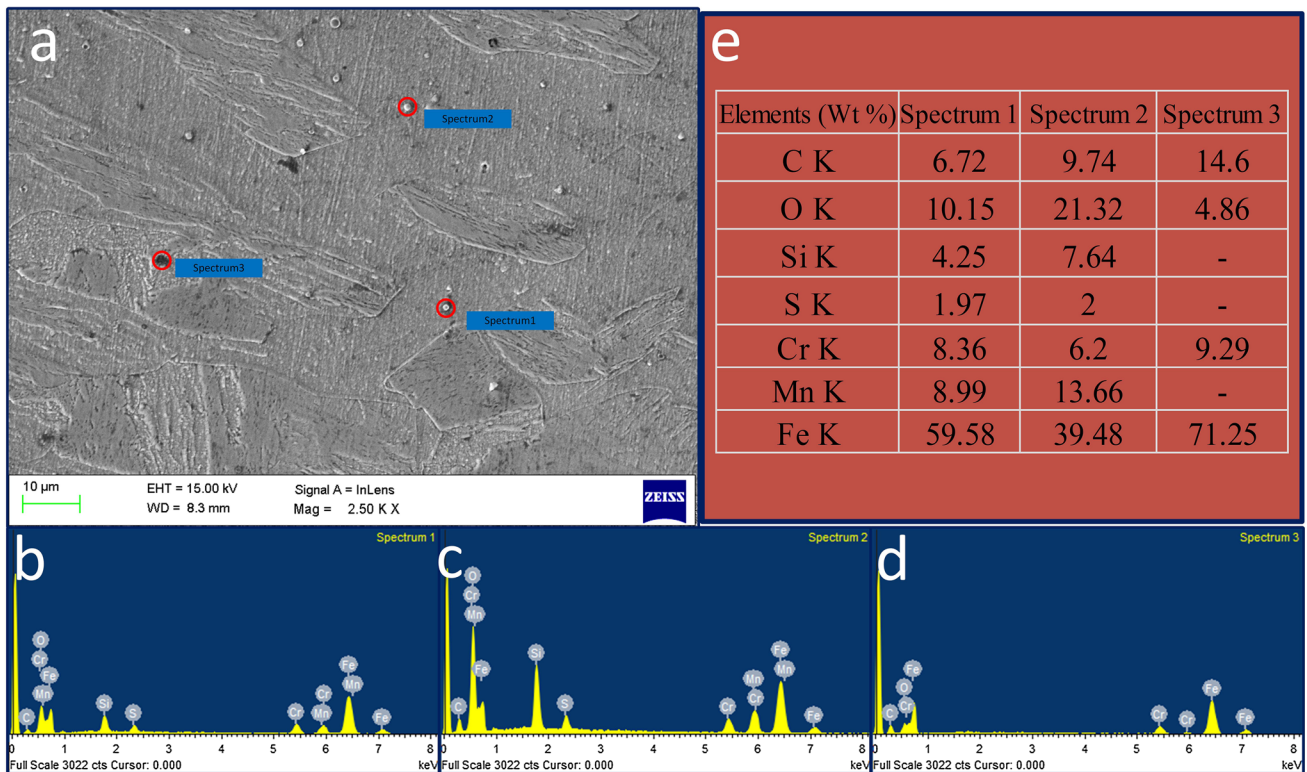
Fig. 13 (a) Inclusions present in A-TIG weld fusion zone, (b-d) EDS pattern of spectrum 1-3, respectively, (e) elemental distribution in the respective spectrums

which are due to the flux during A-TIG welding, may not reduce the corrosion resistance directly, but they could support other inclusions, like sulfides, in creating corrosion-susceptible spots.

5. Conclusions

1. Corrosion resistance of the A-TIG weld fusion zone was significantly affected by the activating flux. However, it was controlled using the proper welding process parameters. The E_{corr} for sample S1 ($-$ 358 mV) was found to be better than the corresponding value for the base metal ($-$ 372 mV).

2. The corrosion resistance of SS 409's A-TIG weld fusion zone increased with the welding current, while it decreased with the welding speed and the flux coating density. The minimum and maximum corrosion resistances (E_{corr}) were observed in the weld fusion zone belonging to sample S7 ($-$ 890 mV) and to sample S1 ($-$ 358 mV), respectively.

3. The corrosion rate of the SS 409's A-TIG weld fusion zone decreased with the welding current, while it increased with the welding speed and the flux coating density. The minimum corrosion rate (mpy) was observed in the weld fusion zone of sample S10 (1.06 mpy), which was welded with a welding current of 230 A, a welding speed of 120 mm/min, and a flux coating density of 1.40 mg/cm^2.

4. The A-TIG weld fusion zone near the fusion boundary showed greater sensitivity to corrosion compared to the

weld center as determined during the potentiodynamic polarization tests.

References

1. T. Balusamy, S. Kumar, and T.S.N. Sankara, Narayanan, Effect of Surface Nanocrystallization on the Corrosion Behaviour of AISI, 409 Stainless Steel, *Corros. Sci.*, 2010, **11**, p 3826–3834
2. C.J. Van Niekerk, M. Du Toit, M.W. Erwee, C.J. Van Niekerk, M. Du Toit, and M.W. Erwee, Sensitization of AISI, 409 Ferritic Stainless Steel During Low Heat Input Arc Welding, *Weld. World*, 2012, **5**, p 54– 64
3. A.K. Lakshminarayanan and V. Balasubramanian, Characteristics of Laser Beam and Friction Stir Welded AISI, 409M Ferritic Stainless Steel Joints, *J. Mater. Eng. Perform.*, 2012, **4**, p 530–539
4. A.K. Lakshminarayanan, K. Shanmugam, and V. Balasubramanian, Fatigue Crack Growth Behavior of Gas Metal Arc Welded AISI, 409 Grade Ferritic Stainless Steel Joints, *J. Mater. Eng. Perform.*, 2009, **7**, p 917–924
5. T.C. Scalise, M.C.L. de Oliveira, I.J. Sayeg, and R.A. Antunes, Sensitization Behavior of Type 409 Ferritic Stainless Steel: Confronting DL-EPR Test and Practice W of ASTM A763, *J. Mater. Eng. Perform.*, 2014, **6**, p 2164–2173
6. R.S. Vidyarthy and D.K. Dwivedi, in *Seventh International Conference on Creep, Fatigue and Creep-Fatigue Interaction*, Indira Gandhi

Centre for Atomic Research, Kalpakkam, Tamil Nadu, India, 19-22 January 2016, pp. 898–903

7. S. Anttila, P. Karjalainen, and S. Lantto, Mechanical Properties of Ferritic Stainless Steel Welds in Using Type 409 and 430 Filler Metals, *Weld. World*, 2013, **3**, p 335–347

8. C.R. Thomas and R.L. Apps, in *Proceedings of American Society for Testing and Materials* (1980), pp. 161–183

9. M. Du Toit, G.T. Van Rooyen, and D. Smith, Heat-Affected Zone Sensitization and Stress Corrosion Cracking in 12% Chromium Type 1.4003 Ferritic Stainless Steel, *Corrosion*, 2007, **5**, p 395–404

10. H. Zheng, X. Ye, L. Jiang, B. Wang, Z. Liu, and G. Wang, Study on Microstructure of Low Carbon 12% Chromium Stainless Steel in High Temperature Heat-Affected Zone, *Mater. Des.*, 2010, **10**, p 4836–4841

11. M. van Warmelo, D. Nolan, J. Norrish, M. van Warmelo, D. Nolan, J. Norrish, M. van Warmelo, D. Nolan, and J. Norrish, Mitigation of Sensitisation Effects in Unstabilised 12%Cr Ferritic Stainless Steel Welds, *Mater. Sci. Eng. A*, 2007, **1-2**, p 157–169

12. R.S. Vidyarthy and D.K. Dwivedi, Activating Flux Tungsten Inert Gas Welding for Enhanced Weld Penetration, *J. Manuf. Process.*, 2016, **22**, p 211–228

13. R.S. Vidyarthy, D.K. Dwivedi, and V. Muthukumaran, Optimization of A-TIG Process Parameters Using Response Surface Methodology, *Mater. Manuf. Process.*, 2017, **April**, p 1–9

14. R.S. Vidyarthy, A. Kulkarni, and D.K. Dwivedi, Study of Microstructure and Mechanical Property Relationships of A-TIG Welded P91-316L Dissimilar Steel Joint, *Mater. Sci. Eng. A*, 2017, **695**, p 249–257

15. R.S. Vidyarthy, D.K. Dwivedi, and M. Vasudevan, Influence of M-TIG and A-TIG Welding Process on Microstructure and Mechanical Behavior of 409 Ferritic Stainless Steel, *J. Mater. Eng. Perform.*, 2017, **3**, p 1391–1403

16. E. Kapilashrami, V. Sahajwalla, and S. Seetharaman, Slag Formation During High Temperature Interactions between Refractories Containing SiO_2 and Iron Melts with Oxygen, *Ironmak. Steelmak.*, 2004, **6**, p 509–513

17. L.R. Bhagavathi, G.P. Chaudhari, and S.K. Nath, Mechanical and Corrosion Behaviour of Plain Low Carbon Dual-Phase Steels, *Mater. Des.*, 2011, **1**, p 433–440

18. J.R. Scully and D.W. Taylor, *ASM Handbook*, Vol 13, 9th ed., ASM, New York, 1987, p 458

19. C.J. van Niekerk and M. du Toit, Sensitization Behaviour of 11-12% Cr AISI, 409 Stainless Steel during Low Heat Input Welding, *J. South. Afr. Inst. Min. Metall.*, 2011, **111**, p 243–256

20. R.A. Luk and J.A. Davis, Intergranular Corrosion in 12 Percent Chromium Ferritic Stainless Steels, *ASTM Int.*, 1978, **656**, p 233–247

21. J.F. Li, Z.W. Peng, C.X. Li, Z.Q. Jia, W.J. Chen, and Z.Q. Zheng, Mechanical Properties, Corrosion Behaviours and Microstructures of 7075 Aluminium Alloy with Various Aging Treatments, *Trans. Nonferrous Met. Soc. China*, 2008, **4**, p 755–762

22. Z. Szklarska-Smialowska and J. Mankowski, Crevice Corrosion of Stainless Steels in Sodium Chloride Solution, *Corros. Sci.*, 1978, **11**, p 953–960

23. J. Zhu, L. Xu, Z. Feng, G.S. Frankel, M. Lu, and W. Chang, Galvanic Corrosion of a Welded Joint in 3Cr Low Alloy Pipeline Steel, *Corros. Sci.*, 2016, **111**, p 391–403

24. S.E. Lott and R.C. Alkire, The Role of Inclusions on Initiation of Crevice Corrosion of Stainless-Steel. 1. Experimental Studies, *J. Electrochem. Soc.*, 1989, **4**, p 973–979

25. J.M. Vitek and R.L. Klueh, Precipitation Reactions during the Heat Treatment of Ferritic Steels, *Metall. Trans. A*, 1983, **6**, p 1047–1055

26. A.S.M. Paroni, N. Alonso-Falleiros, and R. Magnabosco, Sensitization and Pitting Corrosion Resistance of Ferritic Stainless Steel Aged at 800 °C, *Corrosion*, 2006, **11**, p 1039–1046

27. M.L. Greeff, *The Influence of Welding Parameters on the Sensitisation Behaviour of 3Cr12*, University of Pretoria, Pretoria, 2006

28. J.K. Kim, Y.H. Kim, J.S. Lee, and K.Y. Kim, Effect of Chromium Content on Intergranular Corrosion and Precipitation of Ti-Stabilized Ferritic Stainless Steels, *Corros. Sci.*, 2010, **5**, p 1847–1852

29. K.C. Mills and B.J. Keene, Factors Affecting Variable Weld Penetration, *Int. Mater. Rev.*, 1990, **4**, p 185–216

30. L. Antoni and B. Baroux, Cyclic Oxidation Behaviour of Stainless Steels, *Appl. Automot. Exhaust Lines Rev. Métall.*, 2002, **2**, p 177–188

31. D.D.N. Singh, in *COFA-1997* (1997), pp. 169–211